Scientific Research Publishing

Open Journal of Modern Hydrology, 2022, 12, 74-93
https://www.scirp.org/journal/ojmh
ISSN Online: 2163-0496
ISSN Print: 2163-0461

Microphysical and Dynamical Climatology of Precipitating Systems Inferred by Weather Radar Polarimetric Measurements in Brazil

Augusto José Pereira Filho, Felipe Vemado

Departamento de Ciências Atmosféricas; Instituto de Astronomia, Geofísica e Ciências Atmosféricas; Universidade de São Paulo, São Paulo, Brazil
Email: augusto.pereira@iag.usp.br, fvfelp@gmail.com

How to cite this paper: Pereira Filho, A.J. and Vemado, F. (2022) Microphysical and Dynamical Climatology of Precipitating Systems Inferred by Weather Radar Polarimetric Measurements in Brazil. *Open Journal of Modern Hydrology*, **12**, 74-93.
https://doi.org/10.4236/ojmh.2022.122005

Received: February 10, 2022
Accepted: April 9, 2022
Published: April 12, 2022

Abstract

This work presents the climatology of the microphysics and the dynamics of weather systems in two coastal areas of São Paulo and the Espírito States at high spatial-temporal resolution as measured by two dual Doppler weather radars during the summer and early fall of 2015. Averages and respective standard deviations of polarimetric variables, namely, reflectivity (Z), differential reflectivity (Z_{DR}), differential phase (ϕ_{DP}), specific differential phase (K_{DP}), copolar correlation coefficient (ρ_{oHV}), radial velocity (V_r), and the spectral width (W) were obtained within a 240-km range on plan position indicator (PPI), constant altitude plan position indicator (CAPPI) and vertical cross-sections to analyze overall horizontal and vertical precipitation microphysics and mesoscale circulation of prevailing weather systems, and their peculiarities over coastal and oceanic, and urban and rural areas. Overall, raindrops tend to be larger over the Metropolitan area of São Paulo from the surface to up to 6 km altitude indicating more vigorous updrafts caused by the heat island effect and the local sea breeze. The vertical microphysical structure is remarkably distinct over the Metropolitan Area of São Paulo (MASP) where thunderstorms can reach 20-km altitude in summertime under sea breeze and heat island effects. On the other hand, there is a dominancy of smaller drop sizes though larger ones observed close to the surface by the coast of Espírito Santo and at the land-ocean interface influenced by the local low-level jet and oceanic-type CCN. Convective cells tend to be smaller associated with Easterlies and more organized with Westerlies. The results indicate distinct features on hydrometeor types and circulation characteristics under these different surface and boundary-layer conditions in close agreement with previous results in the literature.

Keywords

Dual Doppler Weather RADAR, Microphysics, Climatology, Atlantic Ocean

1. Introduction

[1] has made a thorough review of the polarimetric weather radar technology evolution from the 70s to the mid-90s used across the world and for a myriad of operational and science applications. These include climatological studies of the mesoscale weather systems. Murillo *et al.* [2] analyzed 23-yrs of data on severe hail over the Great Plains of the USA based on radar measurements and reanalysis data and concluded that it is useful to validate datasets and to improve modeling. Similar weather radar hail climatology based on a 55 dBZ reflectivity threshold for hail combined with lighting data has been carried out by Junghänel *et al.* [3] with a 10-yr database of hail events in Germany. Surowiecki and Taszarek [4] obtained the lifespan, morphology, and seasonal frequency of mesoscale convective systems (MCSs) and Derechos based on a 10-yr radar-based climatology for Poland and indicated it is a starting point to study warm-season precipitation for water resources and agriculture of Europe. Goudenhoofdt and Delobbe [5] performed a 10-yr climatology of storms in Belgium based on C-band weather radar measurements at 5-min intervals. They analyzed over a million storms to obtain overall statistics on periods, duration, direction, and speed of storms. Burcea *et al.* [6] utilized a 15-yr weather radar database over the Prut River Basin between Romania and Moldova to characterize the span, duration, direction, and speed of convective storm activity over that basin aiming at assessing the risks associated with severe weather episodes. Lengfeld *et al.* [7] derived climatology of hourly and daily precipitation accumulation estimated by the weather radar network of Germany in a 16-yr weather radar database and concluded that the recurrence of heavy precipitation events is affected by the topography. More recently, Kreklow *et al.* [8] have shown the importance of an improved weather radar quantitative precipitation estimation (QPE) by reanalyzing estimates integrated into ground measurements to remove common radar artifacts, orographic, winter precipitation, and range attenuation.

Kingfield *et al.* [9] analyzed 5-yr gridded weather radar rainfall estimation data to show the effect of the area of the four USA cities on the development of thunderstorms and concluded that larger cities might augment thunderstorms frequency and intensity downwind of the city. Vemado and Pereira Filho [10] observed similar characteristics in the Metropolitan Area of São Paulo (MASP), Brazil under heat island and sea breeze effects. Ihadua and Pereira Filho [11] used an X-band mobile weather radar to analyze the impacts of urban heat island (UHI), sea breeze, and baroclinic effects on thunderstorms microphysics in the MASP. Wu *et al.* [12] used a surface network of rain gauges in South China over a 46-yr period starting in the early 70s and found significant changes in hourly precipitation extremes related to urban effects. Davis and Parker [13] conducted a 4-yr weather radar climatology of tornadic and nontornadic vortices in high-shear and low-CAPE over the mid-Atlantic and southeastern USA and showed distinct magnitudes of the radial shear but range limitations and

very short lead times and concluded that a denser weather radar network is required to nowcasting tornadic thunderstorms.

Hadi *et al.* [14] studied sea breeze circulation in Jakarta, Indonesia, based on boundary layer radar measurements and satellite datasets. The climatology included inland horizontal extent and topographic effects. The author pointed out that the available measurements at that time were not sufficient to refine the results. Wilson *et al.* [15] conducted a polarimetric weather radar experiment in Queensland, Australia in February 2008 and January and February 2009 to study the raindrop size variability in maritime and continental clouds. They analyzed the differential reflectivity Z_{DR} and aerosol concentrations obtained with an onboard probe on an aircraft. The results indicated the differences in raindrop size over land and the ocean with high (lower) aerosol concentrations, long air trajectories, fast (slow) cloud-top growth, higher (lower) cloud tops, and higher (lower) Z_{DR}. The authors proposed further experiments with additional polarimetric weather radars for Dual-Doppler weather radar wind retrieval of vertical motions. Bumke and Seltmann [16] conducted a more extensive measurement campaign of 1-minute drop size sampling with an optical disdrometer placed in several sites over land, coastal areas, semi-enclosed seas, and open sea and found no differences in drop size spectra between continental and maritime areas, but at longer drop spectra time integration.

Xu and Zipser [17] analyzed a 13-yr times series of reflectivity measurements onboard the Tropical Rainfall Mission Satellite (TRMM) to study the vertical structure of deep convection over continents, monsoon areas, and oceans and found significant microphysical structures within continental rainfall that are more intense due to mixed-phase microphysics, less remarkable for monsoon and least for oceanic convection. The main differences in the structure of storms are due to the mixed-phase updrafts and microphysics, rather than the cloud depth or ice depth. More recently, Radhakrishna *et al.* [18], based on more advanced DSD estimates of the global precipitation measurement dual-frequency precipitation radar, studied regional differences in raindrop size distribution within the Indian subcontinent and nearby seas between 2014 and 2018. Among the main finds, they concluded that microphysical and dynamical processes change the DSDs of continental rain.

The above body of research work on precipitation climatology anchored on remote sensing, mainly weather radars of variable technologies and platforms have allowed a broader and deeper understanding of mesoscale convective systems at long and very high spatial-temporal resolution. In the present work, two twins Dual Doppler S-band weather radar systems installed one near the coast of São Paulo State and another by the coast of Espírito Santo State are used to characterize and contrast summer convection over continental and maritime areas, rural and urban areas, and orographic influences during the 2015 warm season. The two SPOL datasets are used to characterize hydrometeors of convective systems under different boundary-layer conditions over land, ocean, urban and ru-

ral areas of São Paulo, and the Espírito States as shown in Figure 1. The hydrometeor types and associated microphysics and dynamics are examined by employing polarimetric variables such as Z_{DR} (dB) and K_{DP} (deg·km^{-1}) to analyze CCN (ESWR) and differential heat island effects (SPWR) under those boundary layer types. The objective is to identify possible boundary layer effects on cloud microphysics and dynamics as well as the resulting rainfall rates and circulations about them.

2. Materials and Methods

2.1. Weather Radars

The São Paulo Weather Radar (SPWR) and the Espírito Santo Weather Radar (ESWR) are both dual-polarization S-band Doppler weather radars installed in

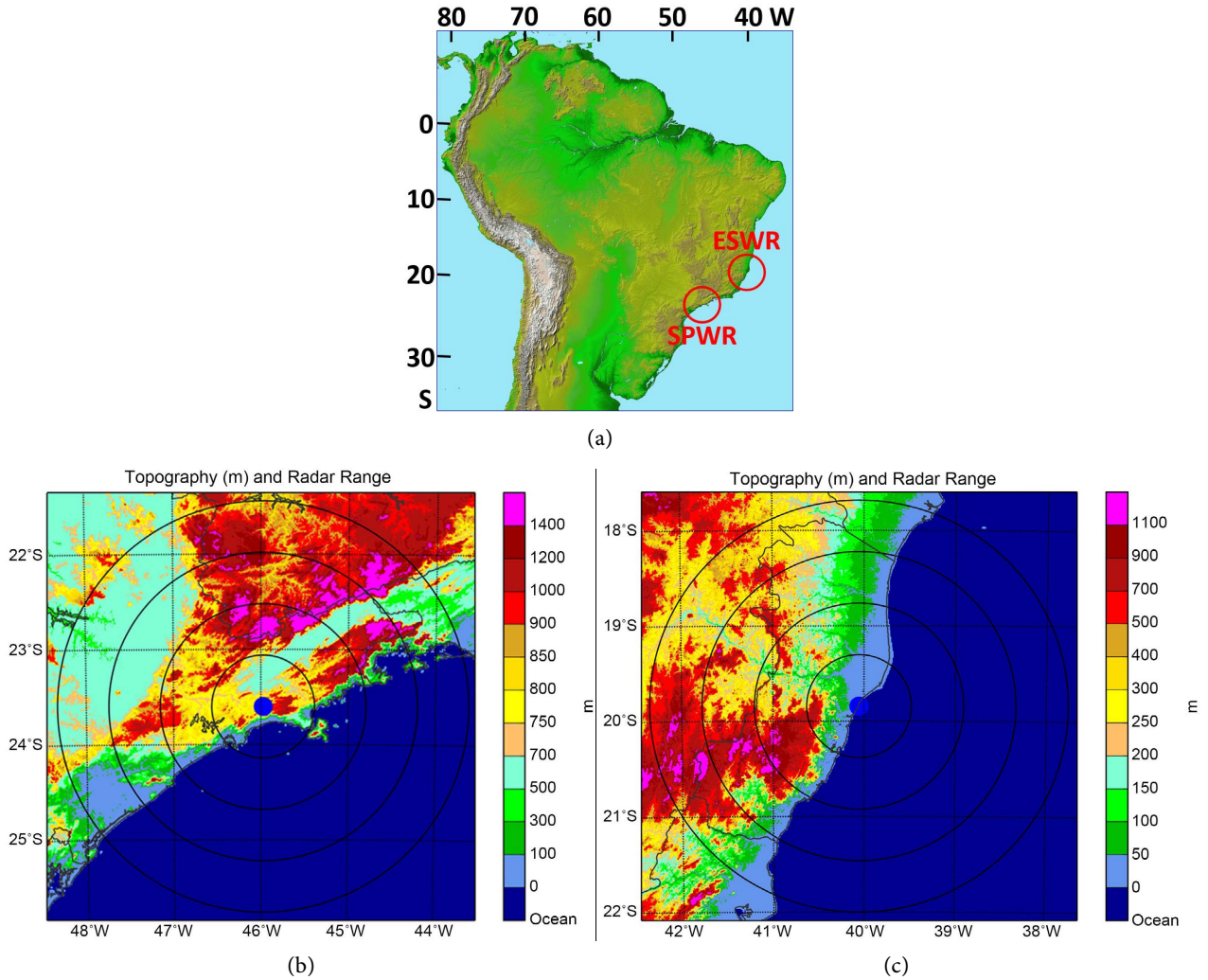

Figure 1. Topographic map of South America (a). Red circumferences are the location with the location of the surveillance area (240-km radius) of the S-POL Weather radars in São Paulo—SPWR (b) and Espírito Santo—ESWR (c) States, Brazil. Latitudes, longitudes, and altitudes are also indicated. Altitudes are shown in colors from low (dark green) to high (brown). The main topography features are the Brazilian high plains centered at (50W, the 20S), the Amazon Basin (55W, 5S), and the La Plata Basin (60W, 25S). Source: NASA/JPL/NIMA.

Salesópolis City, São Paulo State (**Figure 1(b)**) and Aracruz City, Espírito Santo State (**Figure 1(b)**) to survey weather systems within 240-km range. Complete volume scans are obtained every 5-min. at eleven elevation (SPWR) and six elevations (ESWR) angles to monitor clear air and rain conditions at arbitrary constant elevation (PPI) and constant altitude plan position indicator (CAPPI), and cross-sections (RHI) of polarimetric variables. They are briefly described below. Weather radar basics are found in Battan and Isaac [19] while dual-polarization radar characteristics are in Doviak and Zrnic [20].

Both SPWR and ESWR have identical features and their main characteristics are described in Pereira Filho *et al.* [21]. The polarimetric variables are measured horizontally and vertically simultaneously: 1) The horizontal (Z_H) and vertical (Z_V) effective reflectivity ($mm^6 \cdot m^{-3}$). Hydrometeors such as is raindrops, hail, graupel and snow have different backscatter cross-sections and concentrations within the radar beam volume. Since Z_H and Z_v vary from 0 to 10^6 $mm^6 \cdot m^{-3}$, it is converted to $10\log_{10} Z(\mathrm{dBZ})$. Only Z_H was used in this work; 2) Differential Reflectivity (Z_{DR}) is the logarithmic ratio between Z_H and Z_V with units of (dB); 3) Phase differential (f_{DP}) is the difference between the electromagnetic wave phase (˚) emitted and received horizontally and the one emitted and received vertically. It increases with distance as the radar beam pulse goes through the hydrometeors within the clouds; 4) Specific phase differential (K_{DP}) is the radial derivative of f_{DP} between adjacent beam gates; 5) Copolar correlation (r_{oHV}) is the lag zero correlation between the horizontal and vertical polarization signals at a given gate; 6) The radial velocity (V_R) is derived from the Doppler effect and measures the speed ($m \cdot s^{-1}$) of a target moving away (+) or towards (−) the radar and; 7) Spectral width (W) is the variance of the radial wind ($m \cdot s^{-1}$). The raw radar data is in spherical coordinates: antenna elevation angle, azimuth angle, and beam gate volume distance from the radar.

2.2. Datasets and Statistical Analysis

The SPWR and the ESWR datasets recorded between January to April 2015 and December 2014 to April 2015, respectively, were used in this research. The SPWR is installed at 916 m altitudes while the ESWR is at sea level. Volume scans are performed every 5 minutes for both radars but six (ESWR) and eleven (SPWR) elevation angles. So, the SPWR might have sampling issues given its faster antenna rotation.

The lowest PPI and fixed cross-sections of non-null polarimetric variables were used to obtain time averages and the respective standard deviations (′) of the polarimetric variables to analyze horizontal and vertical structures of weather systems, respectively. Time averages and standard deviations of non-null data were obtained for Z (dBZ), K_{DP} ($deg \cdot km^{-1}$), Z_{DR} (dB), R_{OHV}; V ($m \cdot s^{-1}$), and W ($m \cdot s^{-1}$). This approach was used to identify persistent microphysical and dynamical features of summer convection and radar artifacts caused by antenna rotation, ground clutter, anomalous propagation, etc.

2.3. Synthetic Hydrometeor Classification

The definition of weather radar polarimetric variables and bulk hydrometeor classification based on polarimetric measurements are found in Straka *et al.* [22] and Ihadua and Pereira Filho [11]. A summary of Straka *et al.* [22] typical polarimetric thresholds for main hydrometeor types is shown in **Table 1**. They are used in this work to qualitatively analyze different hydrometeor statistics.

3. Results

The radar beam elevation is at 1.0 deg and 1.3 deg elevations for the SPWR and ESWR, respectively. Roughly, the altitude of the PPI is at 2-km, 4-km, and 8-km in the 60-km, 120-km, and 240-km ranges, respectively. Radar vertically pointing measurements of the melting layer by Pereira Filho [23] showed that the 0˚C isotherm is at 3.5 km altitude in eastern São Paulo State. Thus, in general, warm, mixed, and cold microphysics have a higher probability of occurrence between 0 km to 60-km, 60-km to 120-km and beyond the 120-km range, respectively.

Figure 2 and **Figure 3** show the lowest PPI averages (left) and respective standard deviation (right) of non-null polarimetric variables measured by SPWR and by ESWR, respectively. **Figure 2(a)** and **Figure 3(a)** are for the reflectivity Z fields. Both weather radars are affected by ground clutter contamination by mountains (**Figure 1(a)**), beam blockage (metallic structures and trees (SPWR) at the near field range, and far-field range (ESWR) caused by mountains westward (**Figure 1(b)**).

In **Figure 2(a)**, $\overline{Z}$ > 28 dBZ near the ground clutter and at Mantiqueira Mountain Range and at far ranges over the continent $\overline{Z}$ ~ 20 dBZ. On the other hand, over the Atlantic Ocean $\overline{Z}$ ~ 14 dBZ. Close to the SPWR the is 6 dBZ < $\overline{Z}$ < 14 dBZ due to clutter filtering. From 0 km to 40 km range Z' ~ 15 dBZ mainly due to drop spectra variation near surface ground and Z' ~ 6 dBZ above the 200 km range due to cold microphysics near cloud tops. There are bean blocking features at about the 180˚ azimuth and also three others around the 90˚ azimuth. The variance of reflectivity decreases away from the SPWR due to the distance effect, bean filling and cold microphysics at higher altitudes. One might notice that $Z'_{continent} > Z'_{ocean}$ at far ranges are related to lower cloud tops. Z' ~ 6 dBZ over the ground clutter by mountain ranges. The increase of $\overline{Z}$ at mid

Table 1. Hydrometeor types and respective polarimetric thresholds for reflectivity Z (dBZ), differential reflectivity ZDR (dB), specific differential reflectivity KDP (km^{-1}), and the correlation coefficient ROHV. Source: Straka *et al.* [22].

Hydrometeor Type	Polarimetric variable			
	Z_H (dBZ)	Z_{DR} (dB)	K_{DP} (km^{-1})	R_{oHV}
Rain	<60	>0	>0	>0.95
Hail	45 - 80	−2 to 0.5	−0.5 to 1	<0.97
Hail/Graupel	20 - 50	−0.5 to 2	0 to 1.5	>0.95
Rain/Hail	45 - 80	−1 to 6	−0.4 to 0.9	<0.95
Snow	<45	−0.5 to 6	−0.6 to 1	>0.5

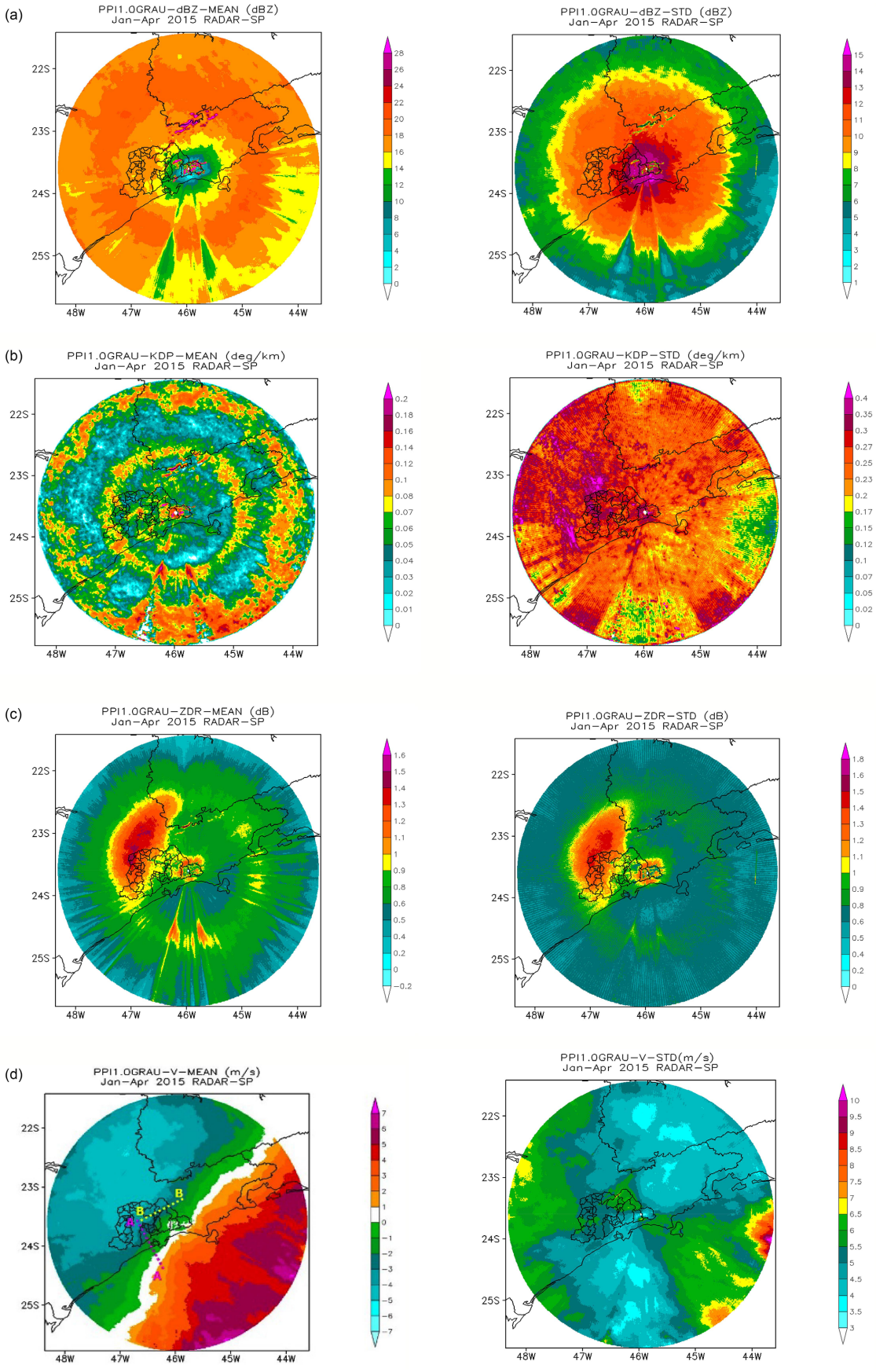
(a)
PPI1.0GRAU−dBZ−MEAN (dBZ)
Jan−Apr 2015 RADAR−SP
PPI1.0GRAU−dBZ−STD (dBZ)
Jan−Apr 2015 RADAR−SP
(b)
PPI1.0GRAU−KDP−MEAN (deg/km)
Jan−Apr 2015 RADAR−SP
PPI1.0GRAU−KDP−STD (deg/km)
Jan−Apr 2015 RADAR−SP
(c)
PPI1.0GRAU−ZDR−MEAN (dB)
Jan−Apr 2015 RADAR−SP
PPI1.0GRAU−ZDR−STD (dB)
Jan−Apr 2015 RADAR−SP
(d)
PPI1.0GRAU−V−MEAN (m/s)
Jan−Apr 2015 RADAR−SP
PPI1.0GRAU−V−STD(m/s)
Jan−Apr 2015 RADAR−SP
22S
23S
24S
25S
48W
47W
46W
45W
44W

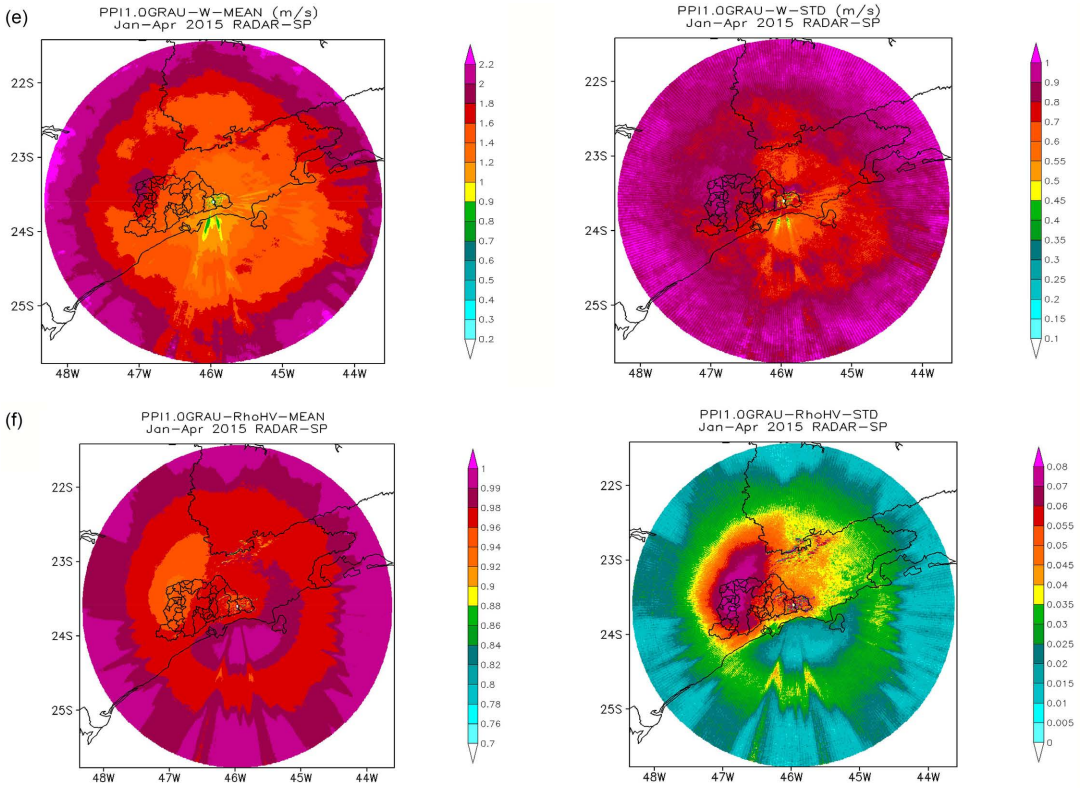

Figure 2. SPWR 1.0 deg. PPIs of mean (left) and standard deviation (right) of non-null polarimetric variables: Z (dBZ) (a); KDP (deg·km^{-1}) (b); ZDR (dB) (c); VR (m·s^{-1}) (d); W (m·s^{-1}) (e) and ROHV (f) for the period of January to April 2015. Geographic boundaries, latitudes and longitudes, and scales are indicated. Cross-sections (aa) (pink dashed line) and (bb) (yellow dashed line) are shown in the radial wind field (bottom-left). The boundaries close to the SPWR are cities within the metropolitan area of São Paulo (MASP). The radius of SPWR surveillance is 240 km.

ranges is caused by melting layer effect is clearly seen in **Figure 2(a)** and $\overline{R_{OHV}}$ (**Figure 2(f)**). It has a broader radial range over the continent that suggests a higher altitude fluctuation of the 0˚ isotherm within the rainy season.

Figure 2(b) shows two rings of $\overline{K_{DP}}$ where 0.14˚·km^{-1} < $\overline{K_{DP}}$ < 0.07˚·km^{-1} at ranges about 120 km associated to the melting layer and 0.18˚·km^{-1} < $\overline{K_{DP}}$ < 0.08˚·km^{-1} above the 200-km range related to cold microphysics. Furthermore, K'_{DP} > 0.3 in between azimuths 270˚ and 360˚. The variability of K'_{DP} tends to be lower over the Atlantic Ocean and in between 0.0.2˚·km^{-1} < K'_{DP} < 0.07˚·km^{-1}. A nucleus of high $\overline{Z_{DR}}$ between 1.0 dB and 1.6 dB is seen in the NW quadrant as well as in Z'_{DR} between 1.0 dB and 1.5 dB that is associated to long-lasting deeper convection and the melting layer with mixed phase microphysics which needs further investigation. The SPWR average radial winds $\overline{V_R}$ in **Figure 2(d)** indicate that the direction of the zero isodop is NE-SW. So, the average winds in the troposphere are Northwesterly and consistent with synoptic-scale 700-hPa and 200-hPa winds shown in **Figure 4**. This prevailing NW flow advects Amazonia moisture specially so during episodes of stationary fronts for several days termed South Atlantic Converge Zone (SACZ), one of the most important circulation systems for the replenishment of the water supply for the Southeast region Pereira Filho *et al.* [24].

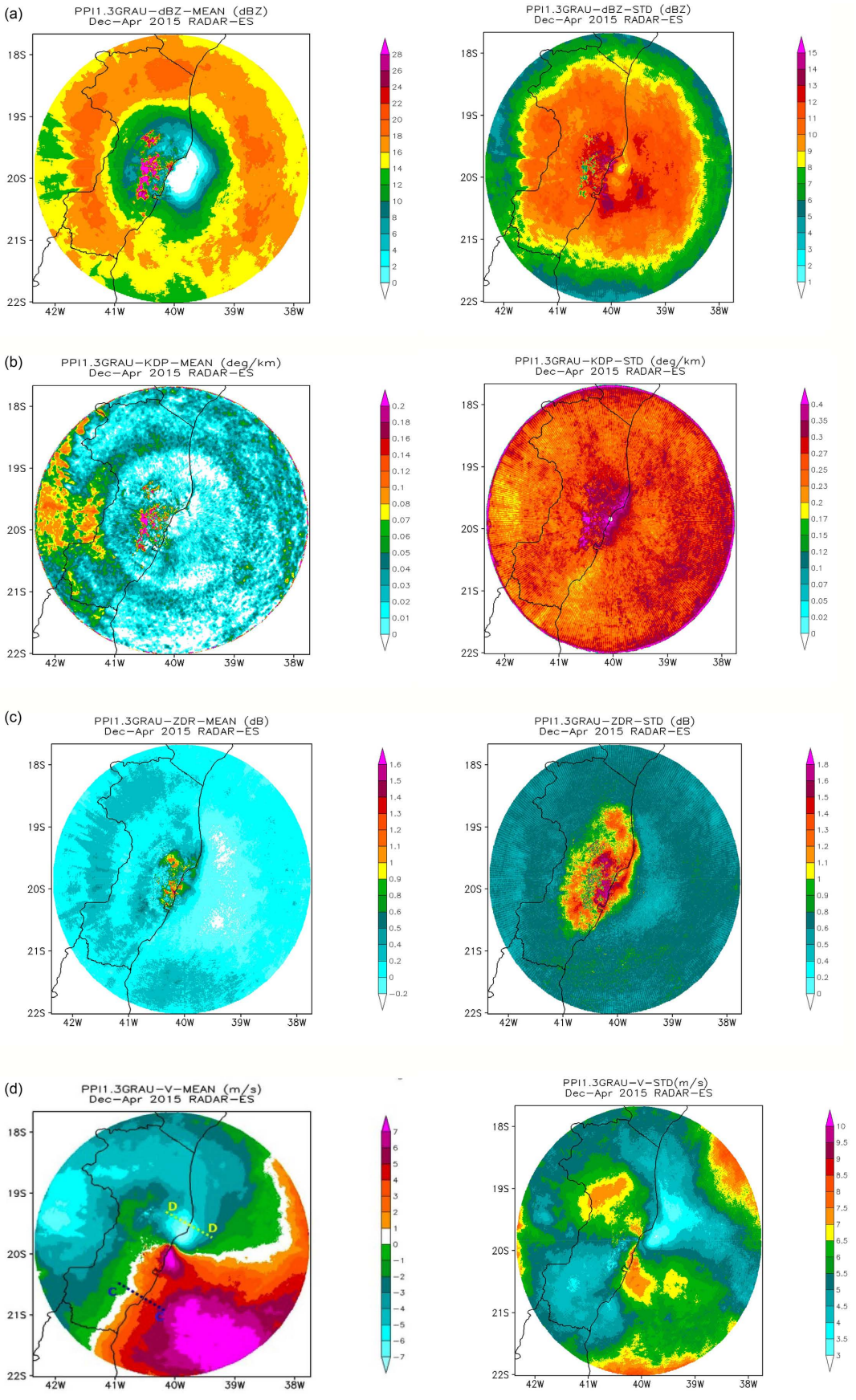
(a)
PPI1.3GRAU–dBZ–MEAN (dBZ)
Dec–Apr 2015 RADAR–ES
PPI1.3GRAU–dBZ–STD (dBZ)
Dec–Apr 2015 RADAR–ES
(b)
PPI1.3GRAU–KDP–MEAN (deg/km)
Dec–Apr 2015 RADAR–ES
PPI1.3GRAU–KDP–STD (deg/km)
Dec–Apr 2015 RADAR–ES
(c)
PPI1.3GRAU–ZDR–MEAN (dB)
Dec–Apr 2015 RADAR–ES
PPI1.3GRAU–ZDR–STD (dB)
Dec–Apr 2015 RADAR–ES
(d)
PPI1.3GRAU–V–MEAN (m/s)
Dec–Apr 2015 RADAR–ES
PPI1.3GRAU–V–STD(m/s)
Dec–Apr 2015 RADAR–ES
18S
19S
20S
21S
22S
42W
41W
40W
39W
38W
D
C

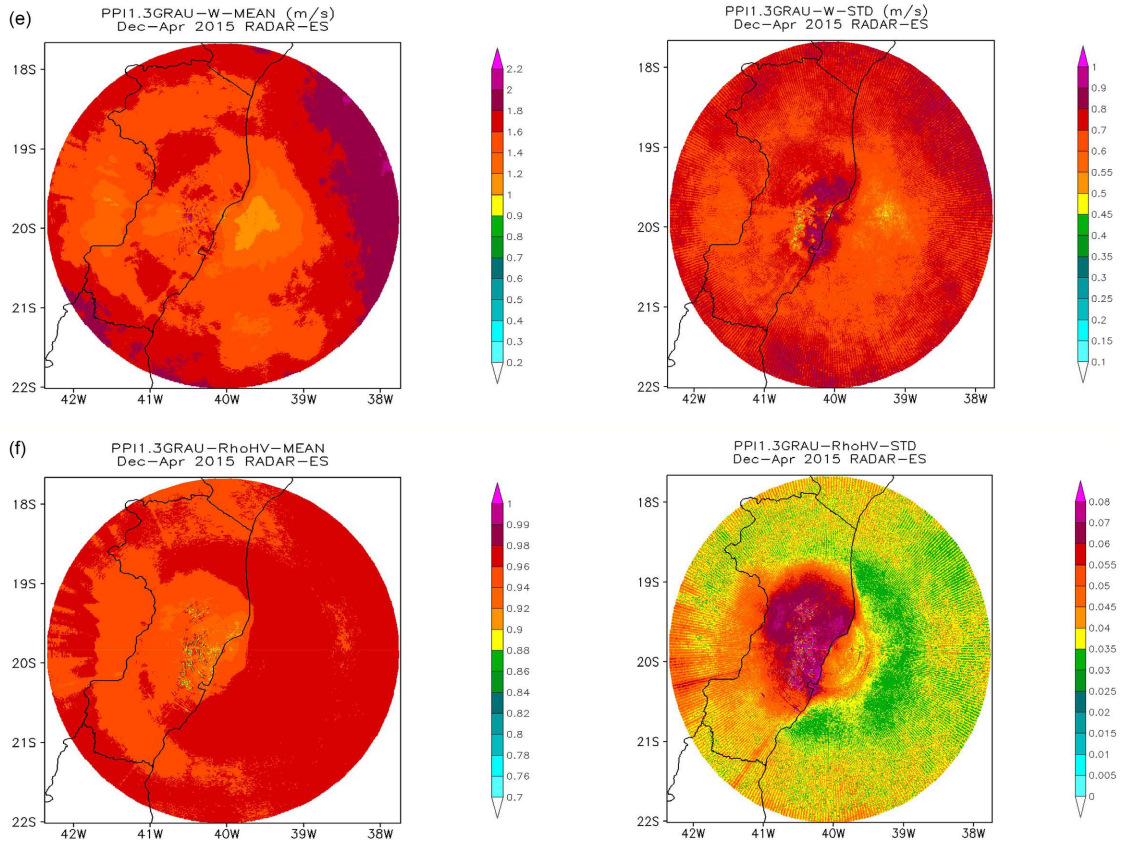

Figure 3. Similar to Figure 2.

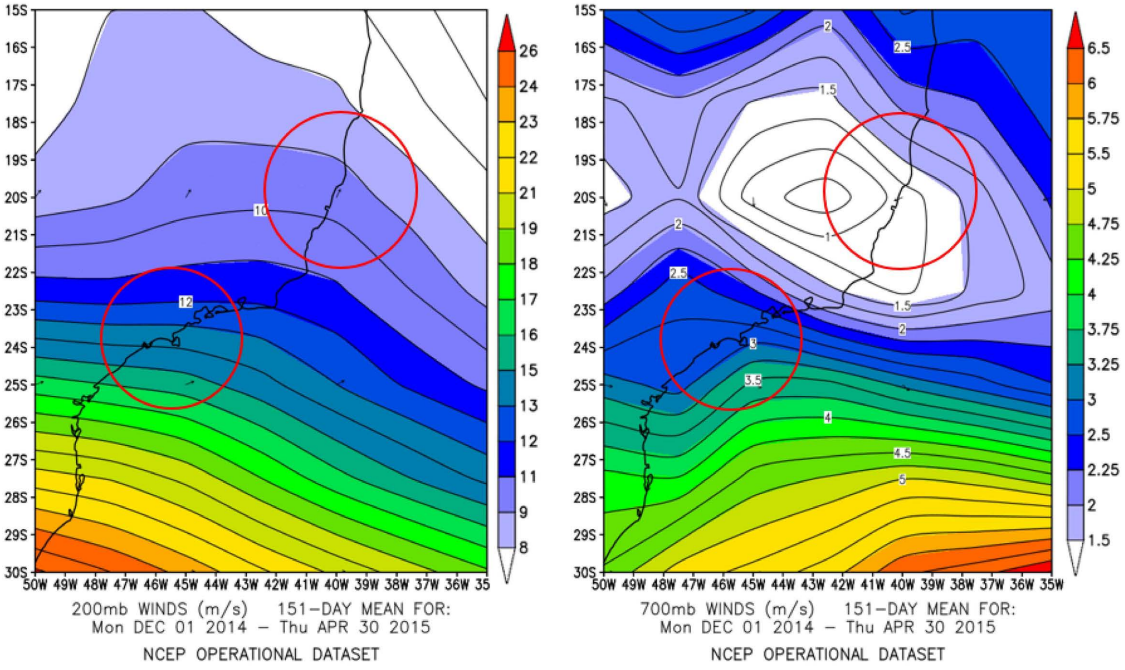

Figure 4. Mean composite of 200-hPa and 700-hPa wind fields between January and April 2015 obtained with NCEP/NCAR Reanalysis System by NOAA Physical Sciences Laboratory. Latitudes, longitudes, geographic boundaries, and wind directions (arrows) are indicated. Surveillance areas of ESWR and SPWR are indicated by the red circumferences. Wind speed in color scales.

The cross-sections (aa) and (bb) in Figure 2(d) were used to examine potentially distinct vertical microphysical structures over continental-ocean (aa) and urban-rural (bb) interfaces. These are analyzed latter in this section by means of $\overline{Z_{DR}}$, Z'_{DR}, $\overline{R_{OHV}}$ and R'_{OHV}. Figure 2(e) shows the average spectral width ($\bar{W}$) and respective standard deviation (W'). This polarimetric variable is associated with the variance of radial winds (V_R) and might be caused by radial wind shear, turbulence and antenna rotation. The average spectral width increases with range or, alternatively, with the altitude, from 0.8 m·s^{-1} to 2.2 m·s^{-1}. The high nucleus of $\bar{W}$ coincides with the one for $\overline{Z_{DR}}$ (Figure 2(c)) with $\bar{W}_{\max}$ ~ 2.2 m·s^{-1} and $W'_{\max}$ ~ 1.0 m·s^{-1}, additional evidence of more vigorous vertical winds and turbulence associated with a preferred region of deeper convective systems.

Figure 2(f) shows the ppis of $\overline{R_{OHV}}$ and R_{OHV}. They are very similar to the ones in Figure 2(c) for $\overline{Z_{DR}}$ and Z'_{DR}. Overall, R_{OHV} varies between 0.9 and 1.0 that indicates the good quality of the polarimetric measurements by SPWR. The lower $\overline{R_{OHV}}$ ~ 0.9 and higher R'_{OHV} ~ 0.08 suggest the impact of mixed phase microphysics in the region that tends to yield larger rain drops Ihadua and Pereira Filho [11]. The $\overline{R_{OHV}}$ field pattern is also similar to $\bar{Z}$ in respect to the melting layer spatial distribution over the continent and over the ocean. R'_{OHV} varies much more over the continent where the diurnal diabatic heating increases buoyancy and deepens convection. Noteworthy, $\overline{R_{OHV}}$ is small in ground clutter areas produced by mountains while R'_{OHV} is higher. This characteristic is caused by the variation of the radar bean elevation under different lower troposphere refractivity that is a function of the vertical gradient of air temperature and moisture content.

Figure 3 shows the statistics of the ESWR that includes the month of December 2014 dataset. The average reflectivity ppi field $\bar{Z}$ in Figure 3(a) varies from 0 dBZ to 28 dBZ. It increases with the distance away from the radar except where ground clutter returns by mountains (westward) are greater than 28 dBZ. The increase of $\bar{Z}$ caused by the bright band forms a more symmetrical belt about the ESWR between 120-km and 200-km range. This suggests that the 0˚ isotherm level is in general higher and variable given also that the ESWR surveys at lower latitudes where the troposphere is deeper. The standard deviation Z' is higher (~14 dBZ) at close ranges and lower (~5 dBZ) at far ranges mainly due to the larger raindrop variation near the ground surface and cold microphysics close to the cloud tops with a much lower complex index of refraction, respectively.

Figure 3(b) for $\overline{K_{DP}}$ and K'_{DP} shows less of a symmetric and almost no existing belt feature associated to the bright band over the Atlantic Ocean. Deeper convection westward over Minas Gerais State with $\overline{K_{DP}}$ ~ 0.16˚·km^{-1} is striking as well as the higher variance K'_{DP} ~ 0.4˚·km^{-1} near the coast within 60-km range. K'_{DP} tends to be more homogeneous K'_{DP} ~ 0.3˚·km^{-1} over the Atlantic Ocean with K'_{DP} ~ 0.05˚·km^{-1}. The statistics of the differential reflectivity $\overline{Z_{DR}}$ and Z'_{DR} is shown in Figure 3(c). $\overline{Z_{DR}}$ is more uniform beyond the 60-km range. It tends to be higher over the continent (~0.4 dB) and lower

over the ocean (~0.02 dB). The standard deviation Z'_{DR} varies from 0.9 dB to 1.8 dB over the continent and close to the coast of Espírito Santo State and from 0.2 dB to 0.9 dB over the ocean, suggesting significantly large raindrop spectra variation. The larger drop sizes over the ocean near the ground surface is a very shallow microphysical feature that might be caused by the LLJ (**Figure 3(d)**) and maritime cloud condensation nuclei (CCN).

Figure 3(d) shows $\overline{V_R}$ and V'_R ppi fields. The zero isodop direction is NE-SW southward of the ESWR and has an inverted S-curvature northward or northwest winds south of the ESWR and warm advection with winds backing with height (Southern Hemisphere) away from the ESWR north of the ESWR, respectively. Radial winds near the ground surface are $\overline{V_R}$ ~ 7 m·s^{-1}. A low-level jet (LLJ) is apparent. The magnitude of the winds is consistent with the ones from the reanalyzes in **Figure 4**. **Figure 3(e)** indicates that the wind spectral width $\overline{W}$ varies between 1 m·s^{-1} and 2.2 m·s^{-1} and W' between 0.4 m·s^{-1} and 1.0 m·s^{-1}. $\overline{W}$ is less radially symmetric but increases with the distance away from the ESWR and varies more close to the coast, especially close to the Tubarão Harbor (Pereira Filho *et al.* [21]), a large by seen 50-km south from ESWR. **Figure 3(f)** shows $\overline{R_{OHV}}$ and R'_{OHV} ppi fields. Apart from ground clutter produced by the mountains westward with $\overline{R_{OHV}}$ ~ 0.9, it indicates the effect of the continental cold microphysics with $\overline{R_{OHV}}$ ~ 0.96 against the ocean warm microphysics with $\overline{R_{OHV}}$ ~ 0.98 virtually everywhere. R'_{OHV} is much higher over the coast (~0.08) than over the ocean (~0.04).

These results indicate significant differences in microphysics over the continent and the ocean in two coastal areas of Brazil that also corroborate previous results briefly described in the introduction but with inedited higher spatial-temporal resolution.

To further analyze the vertical microphysical structure for both the SPWR and the ESWR polarimetric datasets, vertical profiles of $\overline{Z_{DR}}$, Z'_{DR} and $\overline{R_{OHV}}$ and R'_{OHV} were obtained for the cross-sections indicate in **Figure 2(d)** and **Figure 3(d)**. Cross-sections (aa) and (bb) go across continental/ocean and urban/rural surfaces about middle way between them, respectively. On the other hand, cross-sections (cc) and (dd) go across continental/ocean surfaces perpendicular to the coast south and north of the ESWR.

Figure 5 shows the cross-sections of $\overline{Z_{DR}}$, Z'_{DR} and $\overline{R_{OHV}}$ and R'_{OHV} for the (aa) and (bb) directions shown in **Figure 2(d)**. The overall vertical profile (aa) of $\overline{Z_{DR}}$ and ZDR′ indicate very distinct magnitudes below ($\overline{Z_{DR}}$ ~ 1.0 dB) and below ($\overline{Z_{DR}}$ ~ 0.5) the 6-km altitude. Moreover, in cross-section (aa) the maximum $\overline{Z_{DR\,\max}}$ ~ 1.3 dB is below 4-km altitude over the continent and e ocean $\overline{Z_{DR\,\max}}$ ~ 0.8 dB. Similarly, below the 4-km altitude Z'_{DR} ~ 1.2 dB over the continent and Z'_{DR} ~ 0.8 dB over the ocean. This indicates that the rain drop spectra is constitute of large and more variable rain drops over the continent than over the ocean. On the other hand, the vertical profile of $\overline{Z_{DR}}$ and Z'_{DR} of cross-section (bb) are similar but for urban/rural surface boundaries and deeper layers (~8-km).

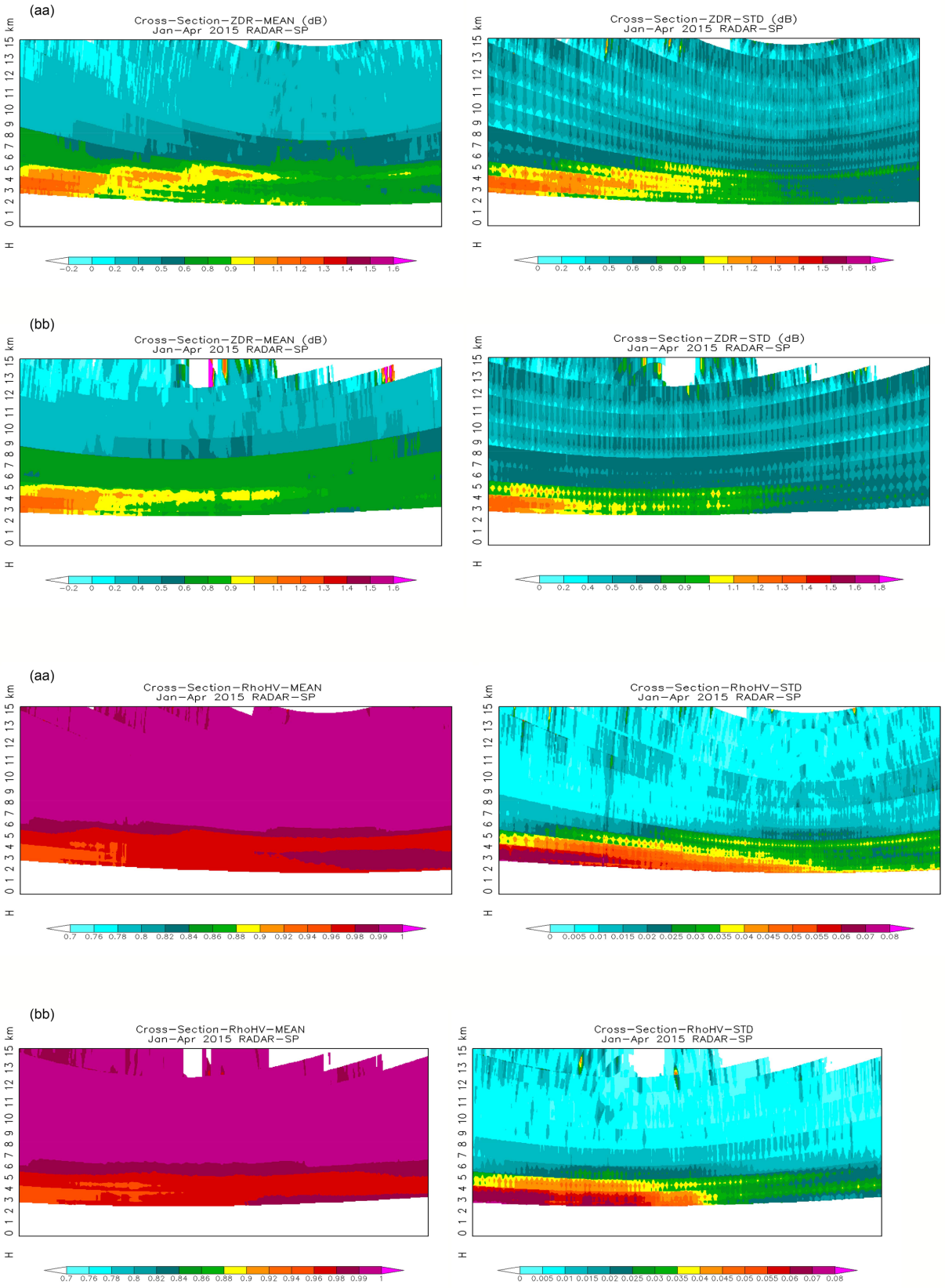

Figure 5. Cross-sections (aa) and (bb) in **Figure 2(d)** for the mean (left) and standard deviation (right) of ZDR (dB) and ROHV for SPWR. Altitudes, longitudes, and color scales are indicated.

Thus, the vertical microphyssummertimeure is remarkably distinct over the Metropolitan Area of São Paulo (MASP) where thunderstorms can reach close to 20-km altitude in summer time under sea breeze and heat island effects (Vemado and Pereira Filho [10]). The average copolar correlation coefficient is almost constant above 6-km altitude with $\overline{R_{OHV}}$ ~ 0.99 in both cross-sections (aa) and (bb) as shown in **Figure 5**. Below the 4-km altitude, is more variable over the continent (R'_{OHV} ~ 0.06) than over the ocean (R'_{OHV} ~ 0.03) as well as over the MASP (R'_{OHV} ~ 0.08) than over rural areas (R'_{OHV} ~ 0.02). Noteworthy, the vertical transition of R_{OHV}, from urban to rural is sharper than from continental to ocean one.

Figure 6 shows vertical profiles indicated in **Figure 3(d)** for the ESWR for cross-sections (cc) (south) and (dd) (north) that go across the coast of Espírito Santo State to the Atlantic Ocean.

Overall raindrops tend to be larger over the Metropolitan area of São Paulo from the surface to up to 6 km altitude indicating more vigorous updrafts caused by the heat island effect and the local sea breeze Pereira Filho *et al.* [25]. The ESWR average Z_{DR} profiles indicate the dominancy of smaller drop sizes though larger ones observed close to surface Northward of ESWR right at the land-ocean interface that is suggested to be influenced by the observed LLJ (**Figure 3(d)**) and Ocean-type CCN. Cells tend to be smaller associated with Easterlies and more organized with Westerlies. Few convective events were monitored and measured with ESWR. Both weather radars have very good quality datasets as indicated by the maximum range of R_{OHV} between 0.96 (**Figure 2(f)**) and 0.98 (**Figure 3(f)**) despite the smaller sampling time for SPWR and spatial resolution for ESWR.

An instance of a convective system monitored by SPWR and ESRW is shown in **Figure 7** and **Figure 8**, respectively. Given the selected cross-sections for the ESWR and the fewer elevation angles, just the second elevation PPI was used. **Figure 7** shows PPIs and cross-sections of a convective episode over MASP at 2025 UTC (1725 LT) on 7 January 2015. This convective system was associated with heat island and sea breeze effects, common features in MASP (Vemado and Pereira Filho [10]). The PPIs of Z (**Figure 7(b)**) and Z_{DR} (**Figure 7(a)**) indicate higher Z and higher Z_{DR} over MASP than elsewhere. Stronger updrafts (**Figure 7(e)**), rich urban CCN, and moisture injected by the sea breeze (**Figure 7(g)**) result in intense rainfall rates Pereira Filho *et al.* [26]. The Z_{DR} cross-section **Figure 7(e)** indicates larger drops up to 7-km altitude, where over-shooting tops in Z are greater than 15-km (**Figure 7(b)**), K_{DP} above 3 deg·km^{-1} (**Figure 7(d)**) with strong radial convergence (**Figure 7(g)**) as well as turbulence indicated by $W > 5$ m·s^{-1} (**Figure 7(h)**).

Figure 8 shows 1.3 deg. PPIs of the polarimetric variables for a case of a South-Eastward moving convective system at 2115 UTC (1815 LT) on 5 February 2015. The reflectivity is higher Z ~ 40 dBZ (**Figure 8(b)**) at the NW quadrant where Z_{DR} ~ 1.5 (**Figure 8(a)**). The region with lower Z ~ 25 dBZ (**Figure 8(b)**) westward and at more distance ranges (higher altitudes) has significantly higher

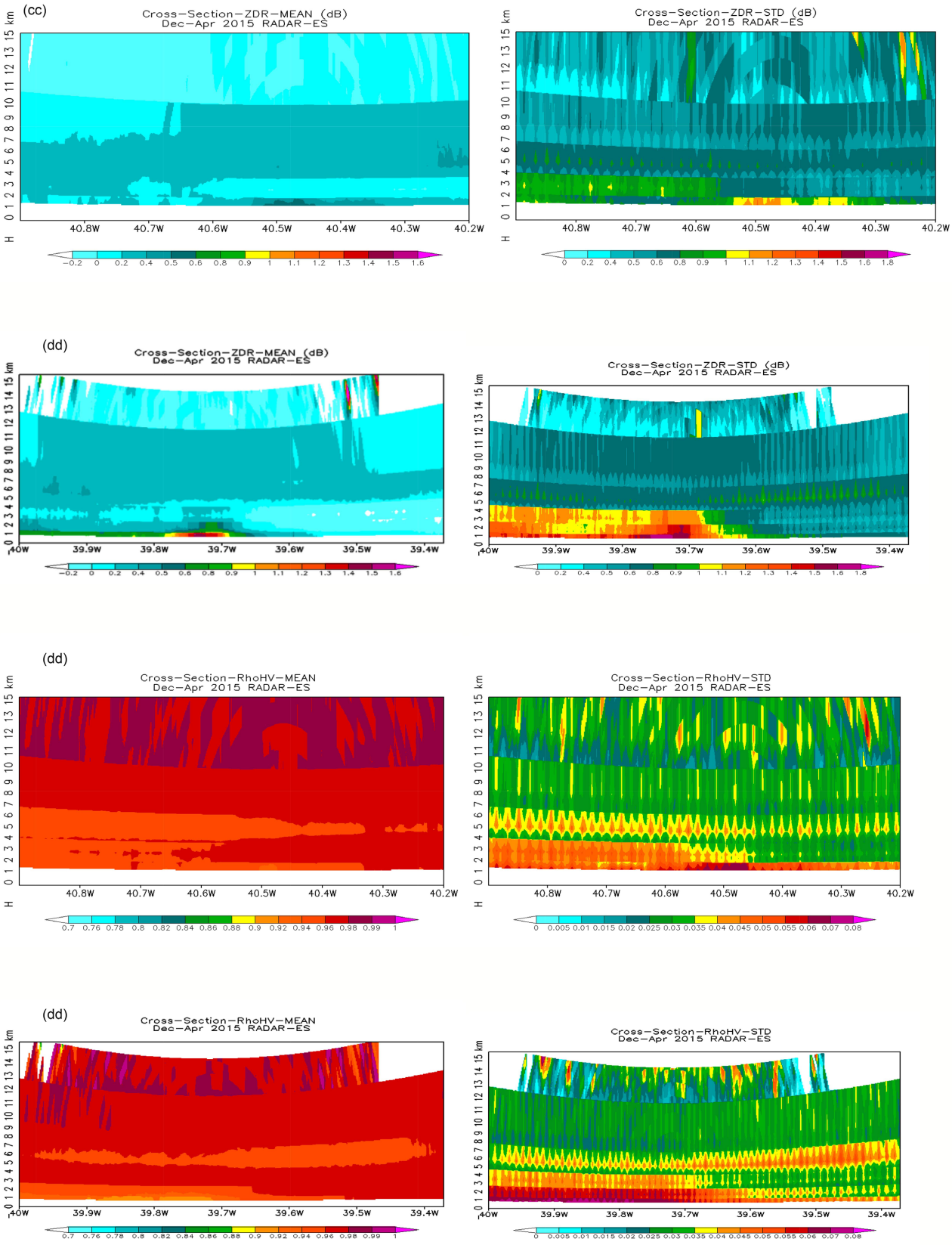

Figure 6. Cross-sections (cc) and (dd) in **Figure 3(d)** for the mean (left) and standard deviation (right) of ZDR (dB) and ROHV for ESWR. Altitude, longitudes, and scales are indicated.

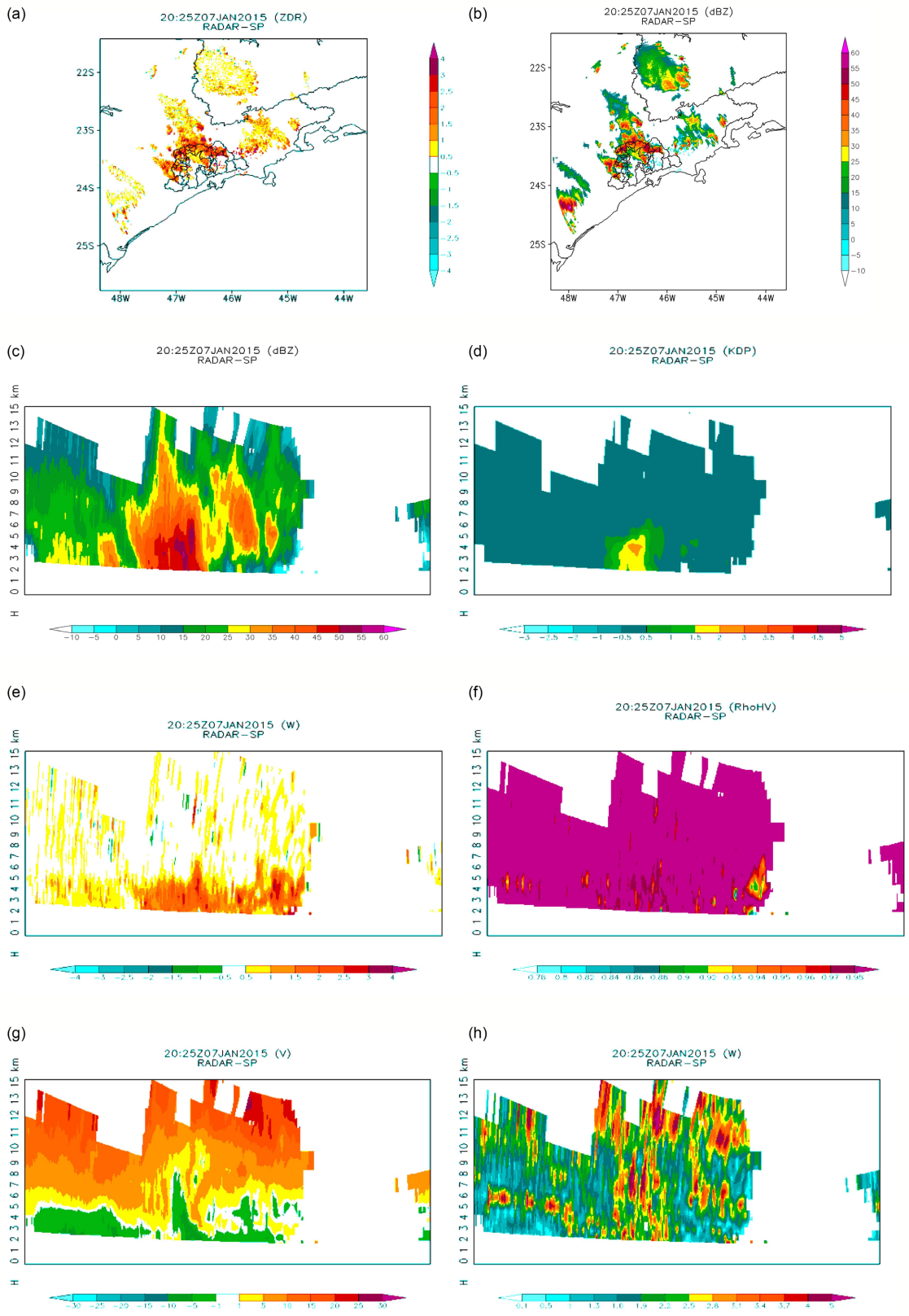

Figure 7. SPWR 1.0 deg. PPIs of ZDR (a) and Z (b) and cross-sections in the direction (bb) in **Figure 2(d)** of Z (dBZ) (c), KDP (deg·km^{-1}) (d), ZDR (dB) (e), ROHV (f); V (m·s^{-1}) (g), W (m·s^{-1}) (h) on 2025 UTC 7 JAN 2015. Geographic boundaries, latitudes, longitudes, heights, and scales are indicated.

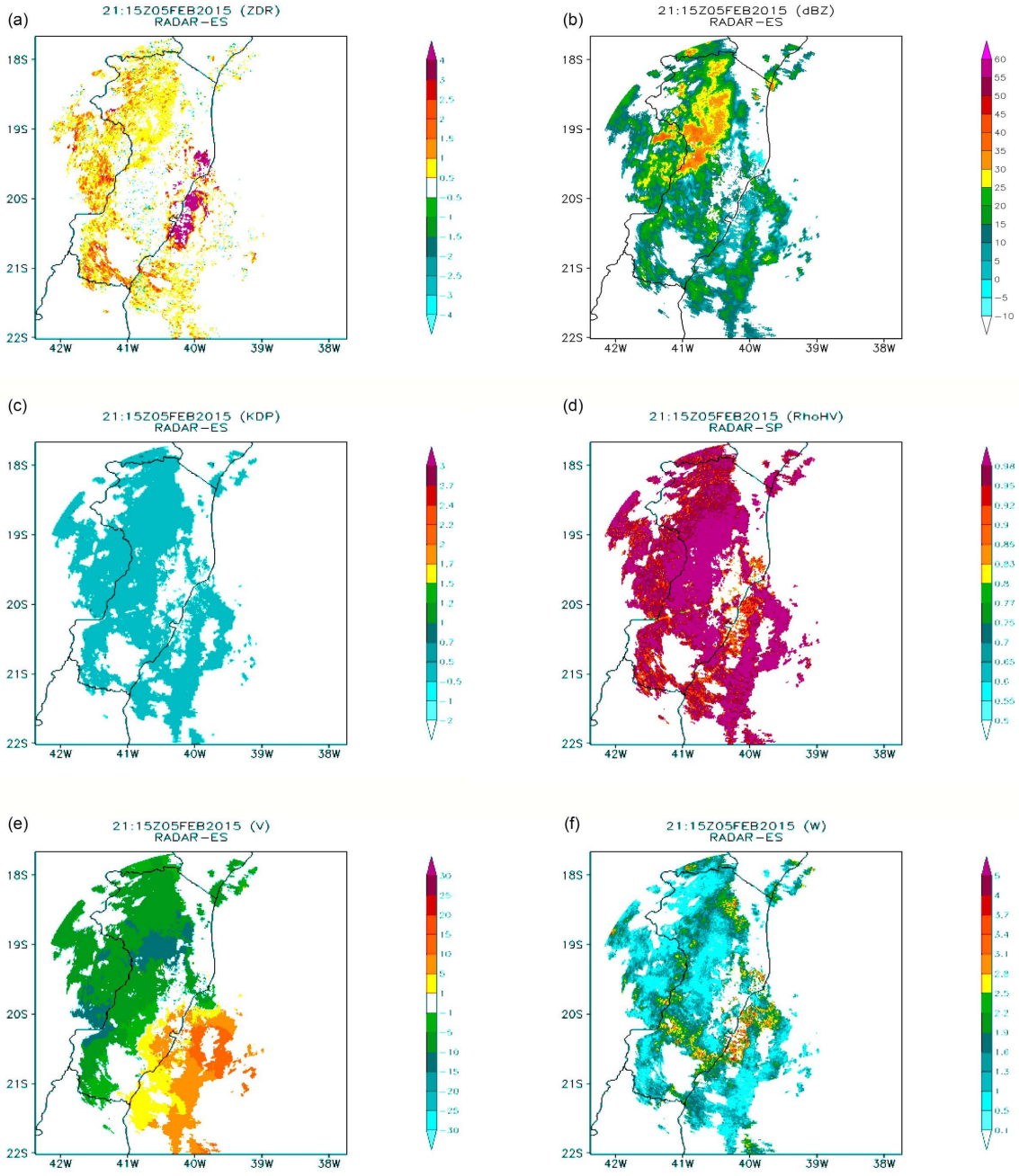

Figure 8. ESWR 1.3 deg. PPIs of ZDR (a); Z (dBZ) (b); KDP (deg·km^{-1} (c); ROHV (d); V (m·s^{-1}) (e), W (m·s^{-1}) (f) on 2115 UTC 5 JAN 2015. Geographic boundaries, latitudes, longitudes, and scales are indicated.

Z_{DR} ~ 1.5 dB (**Figure 8(a)**) and almost constant K_{DP} ~ 0.5˚·km^{-1} (**Figure 8(c)**) indicates a mixed-phase transition at mid-levels. Within the 120-km range, R_{OHV} ~ 0.98 (**Figure 8(d)**) and lower beyond this range with R_{OVH} ~ 0.9 indicates a presence of ice crystals and liquid water. The radial winds (**Figure 8(e)**) are from NW in the upper levels and NE close to the surface. The maximum inbound winds over the continent are V_R ~ 10 m·s^{-1} and the outbound winds V_R ~ 20 m·s^{-1} over the ocean and near coastline close to the surface ground. The spectra width W ~ 3 m·s^{-1} in this region (**Figure 8(f)**) coincides with Z_{DR} > 2 dB. This

feature might be associated with strong winds near the surface that form ocean surface waves and high turbulence that splashes into the airdrops of ocean water. This type of mesoscale convective system shown in **Figure 8** tends to be organized by westward-moving ordinary convection initiated over the Atlantic Ocean (not shown). Despite the higher Z NW of ESWR, Z_{DR} is a larger N-S over the ocean close to shore. Winds ($V_R > 15$ m·s^{-1}) and turbulence ($W > 3$ m·s^{-1}) are stronger in this region where larger drops tend to oscillate more and so reduce ($R_{OHV} < 0.9$).

4. Conclusion

The new SPOL weather radars available in São Paulo and the Espírito Santo States and other regions of Brazil and of the world Zheng *et al.* [27] are very important new data sources to study specific cloud dynamics and microphysics under continental and oceanic and urban and rural environments. For instance, the heat island effect in the MASP produces very deep thunderstorms and is also influenced by the rich urban CCN boundary layer and mixed-phase microphysics with distinct polarimetric variables as seen in the overall features with high values of Z_{DR} at lower levels and negative K_{DP} aloft. The vertical microphysical structure is remarkably distinct over the MASP under sea breeze and heat island effects. Below the 0˚ isotherm, warm microphysics is dominant with distinct characteristics over urban and rural/ocean areas. On the other hand, strong winds and turbulence over the shores of Espírito Santo seem to enlarge drops over the ocean and where maritime CCN is injected though in general shallower convection observed during the summer of 2015. Further studies are being carried out to improve nowcasting tools based on these richer databases available at high spatial-temporal resolution.

Acknowledgements

Support for this research was provided by Conselho Nacional de Desenvolvimento Científico e Tecnológico (CNPq) under grants 302349/2014-6 and 302349/2017-6. The authors would like to thank the Department of Water and Electrical Energy of São Paulo State (DAEE) and Vale S/A for providing SPWR and ESWR datasets, respectively. They are grateful to an anonymous reviewer for improving the manuscript.

Conflicts of Interest

The authors declare no conflicts of interest regarding the publication of this paper.

References

[1] Bringi, V. and Zrnic, D. (2019) Polarization Weather Radar Development from 1970-1995: Personal Reflections. *Atmosphere*, **10**, 714. https://doi.org/10.3390/atmos10110714

[2] Murillo, E.M., Homeyer, C.R. and Allen, J.T. (2021) A 23-Year Severe Hail Climatology Using GridRad MESH Observations. *Monthly Weather Review*, **149**, 945-958. https://doi.org/10.1175/MWR-D-20-0178.1

[3] Junghänel, T., Brendel, C., Winterrath, T. and Walter, A. (2016) Towards a Radar- and Observation-Based Hail Climatology for Germany. *Meteorologische Zeitschrift*, **25**, 435-445. https://doi.org/10.1127/metz/2016/0734

[4] Surowiecki, A. and Taszarek, M. (2020) A 10-Year Radar-Based Climatology of Mesoscale Convective System Archetypes and Derechos in Poland. *Monthly Weather Review*, **148**, 3471-3488. https://doi.org/10.1175/MWR-D-19-0412.1

[5] Goudenhoofdt, E. and Delobbe, L. (2013) Statistical Characteristics of Convective Storms in Belgium Derived from Volumetric Weather Radar Observations. *Journal of Applied Meteorology and Climatology*, **55**, 918-934. https://doi.org/10.1175/JAMC-D-12-079.1

[6] Burcea, S., Cica, R. and Bojariu, R. (2019) Radar-Derived Convective Storms' Climatology for the Prut River Basin: 2003-2017. *Natural Hazards and Earth System Sciences*, **19**, 1305-1318. https://doi.org/10.5194/nhess-19-1305-2019

[7] Lengfeld, K., Winterrath, T., Junghänel, T. and Becker, A. (2019) The Characteristic Spatial Extent of Hourly and Daily Precipitation Events in Germany Derived from 16 Years of Radar Data. *Meteorologische Zeitschrift*, **28**, 363-378. https://doi.org/10.1127/metz/2019/0964

[8] Kreklow, J., Tetzlaff, B., Burkhard, B. and Kuhnt, G. (2020) Radar-Based Precipitation Climatology in Germany—Developments, Uncertainties, and Potentials. *Atmosphere*, **11**, 217. https://doi.org/10.3390/atmos11020217

[9] Kingfield, D.M., Calhoun, K.M., de Beurs, K.M. and Henebry, G.M. (2018) Effects of City Size on Thunderstorm Evolution Revealed through a Multiradar Climatology of the Central United States. *Journal of Applied Meteorology and Climatology*, **57**, 295-317. https://doi.org/10.1175/JAMC-D-16-0341.1

[10] Vemado, F. and Pereira Filho, A.J. (2016) Severe Weather Caused by Heat Island and Sea Breeze Effects in the Metropolitan Area of São Paulo, Brazil. *Advances in Meteorology*, **2016**, Article ID: 8364134. https://doi.org/10.1155/2016/8364134

[11] Ihadua, I.M.T.J. and Pereira Filho, A.J. (2021) On Thunderstorm Microphysics under Urban Heat Island, Sea Breeze, and Cold Front Effects in the Metropolitan Area of São Paulo, Brazil. *Atmospheric and Climate Sciences*, **11**, 614-643. https://doi.org/10.4236/acs.2021.113037

[12] Wu, M.W., Luo, Y.L., Chen, F. and Wong, W.K. (2019) Observed Link of Extreme Hourly Precipitation Changes to Urbanization over Coastal South China. *Journal of Applied Meteorology and Climatology*, **58**, 1799-1819. https://doi.org/10.1175/JAMC-D-18-0284.1

[13] Davis, J.M. and Parker, M.D. (2014) Radar Climatology of Tornadic and Nontornadic Vortices in High-Shear, Low-CAPE Environments in the Mid-Atlantic and Southeastern. *Weather and Forecasting*, **29**, 828-853. https://doi.org/10.1175/WAF-D-13-00127.1

[14] Hadi, T.W., Horinouchi, T., Tsuda, T., Hashiguchi, H. and Fukao, S. (2001) Sea-Breeze Circulation over Jakarta, Indonesia: A Climatology Based on Boundary Layer Radar Observations. *Monthly Weather Review*, **130**, 2153-2166. https://doi.org/10.1175/1520-0493(2002)130<2153:SBCOJI>2.0.CO;2

[15] Wilson, J.W., Knight, C.A., Tessendorf, S.A. and Weeks, C. (2011) Polarimetric Radar Analysis of Raindrop Size Variability in Maritime and Continental Clouds. *Journal of Applied Meteorology and Climatology*, **50**, 1970-1980.

https://doi.org/10.1175/2011JAMC2683.1

[16] Bumke, K. and Seltmann, J. (2012) Analysis of Measured Drop Size Spectra over Land and Sea. *International Scholarly Research Network Meteorology*, **2012**, Article ID: 296575. https://doi.org/10.5402/2012/296575

[17] Xu, W. and Zipser, E.J. (2012) Properties of Deep Convection in Tropical Continental, Monsoon, and Oceanic Rainfall Regimes. *Journal of Geophysical Research*, **39**, L07802. https://doi.org/10.1029/2012GL051242

[18] Radhakrishna, B., Saikranthi, K. and Rao, T.N. (2020) Regional Differences in Raindrop Size Distribution within the Indian Subcontinent and Adjoining Seas as Inferred from Global Precipitation Measurement Dual-Frequency Precipitation Radar. *Journal of the Meteorological Society of Japan*, **98**, 573-584. https://doi.org/10.2151/jmsj.2020-030

[19] Battan, L.J. and Isaac, G.A. (1973) Radar Observation of the Atmosphere. University of Chicago Press, Chicago, 323 p.

[20] Doviak, R.J. and Zrnic, D.S. (1993) Doppler Radar and Weather Observations. Academic Press, Cambridge, 562 p.

[21] Pereira Filho, A., Pereira, J., Vemado, F. and Silva, I. (2015) Operational Hydrometeorological Forecast System for Espírito Santo State, Brazil. *Journal of Hydrologic Engineering*, **22**, E5015003. https://doi.org/10.1061/(ASCE)HE.1943-5584.0001215

[22] Straka, J.M., Zrnić, D.S. and Ryzhkovc, A.V. (2000) Bulk Hydrometeor Classification and Quantification Using Polarimetric Radar Data: Synthesis of Relations. *Journal of Applied Meteorology and Climatology*, **39**, 1341-1372. https://doi.org/10.1175/1520-0450(2000)039<1341:BHCAQU>2.0.CO;2

[23] Pereira Filho, A.J. (2012) A Mobile X-POL Weather Radar for Hydrometeorological Applications in the Metropolitan Area of São Paulo, Brazil. *Geoscientific Instrumentation, Methods and Data Systems*, **1**, 169-183. https://doi.org/10.5194/gi-1-169-2012

[24] Pereira Filho, A.J., *et al.* (2018) A Step towards Integrating CMORPH Precipitation Estimation with Rain Gauge Measurements. *Advances in Meteorology*, **2018**, Article ID: 2095304. https://doi.org/10.1155/2018/2095304

[25] Pereira Filho, A.J., Vemado, F., Peres, F., da Silva Jr., J.R.R. and Tanaka, K. (2013) Measurements of Drop Size Distribution in a Megacity. *AMS 36th Radar Conference*, Breckenridge, CO, 2013, 5 p. https://ams.confex.com/ams/36Radar/webprogram/Paper228510.html

[26] Pereira Filho, A.J., Vemado, F. and Karam, H.A. (2019) Evidence of Tornadoes and Microbursts in São Paulo State, Brazil: A Synoptic and Mesoscale Analysis. *Pure and Applied Geophysics*, **176**, 5079-5106. https://doi.org/10.1007/s00024-019-02276-3

[27] Zheng, S., Wang, G., Huang, X. and Liu, G. (2018) Design and Analysis of Transmitter Charge Switch Assembly Load on Weather Radar Test Platform. *Journal of Geoscience and Environment Protection*, **6**, 51-58. https://doi.org/10.4236/gep.2018.610004